Journal of Alloys and Compounds 967 (2023) 171740

Contents lists available at ScienceDirect

Journal of Alloys and Compounds

journal homepage: www.elsevier.com/locate/jalcom

Effect of heat treatment on microstructure and functional properties of additively manufactured NiTi shape memory alloys

Jia-Ning Zhu [a,*], Weijia Zhu [a], Evgenii Borisov [b], Xiyu Yao [c], Ton Riemslag [a], Constantinos Goulas [d], Anatoly Popovich [b], Zhaorui Yan [a], Frans D. Tichelaar [e], Durga P. Mainali [a], Marcel Hermans [a], Vera Popovich [a,*]

[a] Department of materials science and engineering, Delft University of Technology, the Netherlands
[b] Peter the Great Saint-Petersburg Polytechnic University, Saint Petersburg, Russia
[c] Department of Materials Science and Engineering, Southern University of Science and Technology, Shenzhen, China
[d] Department of Design Production & Management, University of Twente, Enschede, the Netherlands
[e] Kavli Institute of Technology, Quantum Nanoscience, Delft University of Technology, Delft, the Netherlands

ARTICLE INFO

Keywords:
Laser powder bed fusion
NiTi alloys
Heat treatment
Microstructure
Shape memory effect

ABSTRACT

Additive manufacturing of NiTi shape memory alloys has attracted attention in recent years, due to design flexibility and feasibility to achieve four-dimensional (4D) function response. To obtain customized 4D functional responses in NiTi structures, tailorable phase transformation temperatures and stress windows as well as one-way or two-way shape memory properties are required. To achieve this goal, various heat treatments, including direct aging, annealing and annealing followed by aging, were optimized for the Ti-rich NiTi (Ni49.6Ti (at. %)) fabricated by laser powder bed fusion (L-PBF). Microstructural evolution, phase transformation, precipitation and shape memory behaviour were systematically investigated by multiscale correlative microstructural, differential scanning calorimetry analysis and thermomechanical analysis. Based on optimized heat treatments, ~25 K phase transformation temperature windows and ~90 MPa stress windows were achieved for the one-way shape memory effect. Solutionized annealing was found to be the most effective way to improve one-way shape memory degradation resistance, due to the reduction of defects and solid solution strengthening. One of the main findings of this study is that the heterogonous microstructures between hard intergranular Ti_2NiO_x and soft NiTi matrix, induced by solutionized annealing with subsequent aging, result in strain partitioning and enclosing the internal stress state, which was found to promote a pronounced two-way shape memory effect response. The results of this work provide in-depth knowledge on tailoring and designing functional shape memory characteristics via heat treatments, which contributes to expanding L-PBF NiTi application fields, such as biomedical implants, aerospace components, and other advanced engineering applications.

1. Introduction

NiTi alloys, as functional materials, have been widely used in various industrial, high-tech and medical fields [1]. Generally, there are three main functions in NiTi SMAs, including superelasticity, elastocaloric and shape memory effects. Superelasticity and elastocaloric effect both are associated with reversible stress-induced martensitic transformation [2]. Depending on the conditions required for shape recovery, the shape memory effect is divided into the one-way shape memory effect (OWSME) and the two-way shape memory effect (TWSME) [3]. OWSME refers to the ability of a material to remember only one shape. When a material is deformed from its original shape, it can return to its original shape only by heating it above its recovery temperature (austenite finish temperature, A_f)). If the material is deformed below the recovery temperature, it will remain in its deformed shape. TWSME, on the other hand, refers to a material capable to remember two different shapes, where shape changes spontaneously occur during heating and cooling without any external stress [4,5]. Theses attractive functions make NiTi attractive for such smart applications as sensors, actuators, dampers and solid refrigeration [1].

However, the high reactivity and poor machinability of NiTi limit its design complexity, which is essential for smart device design. Laser

* Corresponding authors.
E-mail addresses: J.Zhu-2@tudelft.nl (J.-N. Zhu), V.Popovich@tudelft.nl (V. Popovich).

https://doi.org/10.1016/j.jallcom.2023.171740
Received 29 May 2023; Received in revised form 25 July 2023; Accepted 13 August 2023
Available online 14 August 2023

powder bed fusion (L-PBF), categorized as additive manufacturing (AM), is considered an alternative technique allowing for more design flexibility of smart components [6]. Recently, NiTi with complex topological structures, designed for damping or medical applications, has been successfully fabricated by L-PBF [7,8].

Due to the high heating and cooling rate in L-PBF (up to $\sim 10^6$ K·s^{-1}) [9], steep temperature gradient (in the magnitude of $\sim 10^7$ K·m^{-1}) [10,11], layer-by-layer and track-by-track processing characteristics [12], produce materials having non-equilibrium solidification microstructures, including heterogeneous microstructures, metastable phases, micro-segregations and dislocations [13–15]. For NiTi, such non-equilibrium solidification microstructures affect its phase transformation temperatures and functional behavior. For instance, the compositional ratio of Ni/Ti in the NiTi matrix influences the martensitic phase transformation temperatures [16]. The deviation of matrix composition may result from element segregation or precipitation of second phases, which in turn, affects phase transformation temperatures [17]. Dislocations, associated with anisotropic stress fields [18], are commonly observed in the as-fabricated L-PBF NiTi [11], which impedes martensitic transformation during thermal cycling (decrease in martensite finish temperature) [11] and promotes the stress-induced formation of martensite during superelastic cycling (decrease in plateau stress in the forward transformation) [19].

The non-equilibrium features in L-PBF NiTi imply a possibility to tailor the phase transformation temperature and applied stress windows by controlling its microstructures. Heat treatments, as cost-effective and simple methods, are promising to tailor L-PBF NiTi functional properties. Recently, efforts have been made to study the effect of heat treatment on L-PBF NiTi. Tunable superelasticity and elastocaloric effects were achieved by applying heat treatments to control the precipitation of Ni_4Ti_3 in Ni-rich NiTi [20]. However, most heat treatment-related studies have been focused on Ni-rich NiTi [15,20,21], since the achievable Ni_4Ti_3 phases introduced by aging enhance the superelastic and elastocaloric effects. Until now, there are only very limited studies on the heat treatment responses of L-PBF Ti-rich NiTi [22–24], in which only mechanical properties were investigated. There is still a lack of understanding of the effect of heat-treated microstructures on the shape memory effect. Moreover, the cyclic OWSME and TWSME of heat-treated L-PBF Ti-rich NiTi have never been investigated, which is important for a wide range of engineering applications [25]. Therefore, it is imperative to develop L-PBF Ti-rich NiTi with tunable OWSME and TWSME via applying appropriate heat treatments and understanding the relationship between microstructure and functional properties.

Due to the low crystallographic symmetry of NiTi martensite (B19′), polycrystalline NiTi shows different deformation behavior when applying various deformation modes (including uniaxial tension, compression, and shear) [26]. Especially, NiTi is very sensitive to strain hardening under compression during the SME test [26], which is associated with the generation of a high density of dislocations [27]. By contrast, under tension, there is no significant plastic deformation and a flat stress plateau is observed, which is due to a high mobility of ⟨011⟩ type II twin junction planes of polycrystalline NiTi [27]. It indicates that residual strains or plastic deformation are easier to be accumulated, resulting in shape memory degradation under the cyclic compressive loading condition. Indeed, the superior shape memory effect of L-PBF NiTi was mainly reported for the tensile condition [28–31]. Therefore, it is still challenging for NiTi to achieve a stable shape memory effect under the compressive condition.

In this study, to understand the effect of heat treatments on microstructure evolution, phase transformation behavior and shape memory effect in L-PBF Ti-rich NiTi alloys, for different heat treatment schemes, including solutionized annealing, directly aging and annealing followed by aging, were applied. Nano-scaled structures were investigated by high-resolution transmission electron microscopy. The cyclic compressive-thermomechanical behavior of L-PBF NiTi without and with heat treatments was evaluated after 50 cycles. Finally, NiTi with tunable SME stress and temperature windows were successfully developed based on specific heat treatments. Relationships between microstructure, nano-precipitates and thermomechanical properties (including one-way and two-way shape memory effect) were discussed. Solutionized annealing was found to improve the OWSME degradation resistance, and subsequent aging helped to promote the TWSME response in L-PBE NiTi. To our best knowledge, this is the first systematic multiscale correlative investigation on microstructure, differential scanning calorimetry analysis (DSC), cyclic OWSME and TWSME of heat treated L-PBF Ti-rich NiTi. This work may provide an insightful understanding of designing function-tunable 4D printing NiTi.

2. Materials and methods

2.1. Material processing

The material investigated herein was Ni49.6Ti (at. %) manufactured via L-PBF [28]. The NiTi samples were fabricated using an Aconity3D Midi (Aconity3D GmbH, Germany) machine equipped with a laser source featuring a maximum power of 1000 W and a beam with a Gaussian distribution. A bidirectional scanning strategy with 67° rotation between adjacent layers was implemented for fabricating cylindrical samples (diameter of 13 mm and height of 25 mm) (shown in Fig. 1(a)). Based on our previous optimization [32], the following L-PBF process parameters were used: 250 W laser power (P), 1250 mm/s scanning velocity (v), 120 μm hatch distance (h), 30 μm layer thickness (t) and 80 μm laser beam diameter. The as-fabricated NiTi sample is named AF hereafter.

To investigate the effect of heat treatments on the shape memory effect of Ti-rich L-PBF NiTi, three types of heat treatments were carried out on as-fabricated NiTi, i.e. solution annealing, directly aging and solution annealing followed by aging. Based on the NiTi binary phase diagram, Ni49.6Ti (at. %) is solid when the temperature is lower than 1257 K. To reduce the residual stress and homogenise the microstructure, solutionized annealing was carried out at 1223 K for 5.5 h followed by water quenching, referred to as S hereafter. For the direct aging, samples were held at 623 K for 18 h indicate by A hereafter. For the solution annealing followed by aging, samples were firstly held at 1223 K for 5.5 h and then aged at 623 K for various holding durations (0.5–27 h). The optimized annealing 1223 K-5.5hs followed by aging 623 K-18 hs is named S+A hereafter. To prevent oxidation of NiTi, all samples were placed in stainless steel envelopes filled with argon during heat treatments. Post-process heat treatments details are summarized in Table 1.

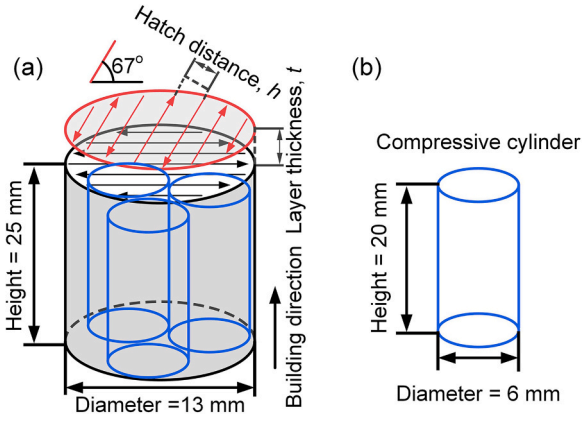

Fig. 1. (a) The schematic of the applied L-PBF scanning strategy and (b) the machined cylinder for compressive tests by EDM.

Table 1
The overview of the post-heat treatments.

Post treatments	Temperature - duration
Directly aging, A	623 K - 18 hs
Solutionized annealing, S	1223 K - 5.5 hs
Solutionized annealing followed by aging, S+A	1223 K-5.5 hs + 623 K-18 hs

2.2. Thermomechanical tests

Thermomechanical compression tests were conducted using a 25 kN MTS 858 Table Top servo-hydraulic test platform. Using a strain control loop, a strain rate of 10^{-4} s^{-1} was employed when loading and unloading were performed. Samples were machined into cylinders with a dimension of ϕ 6 × 20 mm by electrical discharging machining (EDM) (Fig. 1(a)). The strain was measured by a ceramic rod extensometer with a gauge length of 12 mm (MTS model 632.53F-14), which was attached to the samples. The samples were heated up using an induction coil and cooled via three air-blowing nozzles. The temperature was controlled (and monitored) by a K-type thermocouple, spot welded at the middle of the sample. A 3-step gradually increasing strain level test was applied to investigate the critical stress for phase transformation and strain recovery (Fig. 2(a)). "Hard" cyclic tests [33], where the same maximum nominal strain is reached for each cycle (50 cycles with a fixed maximum 4 % strain), were applied to investigate the cyclic SME stability (Fig. 2(b)). Schematics of strain definitions and loading paths for the shape memory effect are shown in Fig. 2(c).

To investigate the two-way shape memory effect, The dilatation of the samples after 50 thermomechanical cycles as a function of temperature is determined using a dilatometer (TMA PT 1000/LT). A k-type thermocouple was spot welded onto the middle of sample. In the study, each sample is initially cooled to 203 K, then heated to 473 K, and finally cooled down to 273 K at a rate of 10 K per minute.

2.3. Microstructural characterization

Before the metallographic examination, samples were ground, polished and tint etched and the detailed procedure can be found in our previous work [11]. The etched microstructures were then examined via a Leica DMI 5000 optical microscope under the polarized light mode. For Vickers hardness measurements, a Durascan microhardness tester (Struers) was used. Polished samples were tested under the main load of 2 kgf (HV_2) with a loading time of 10 s. An average of 10 hardness values for each sample is reported. The series of indents were made at a distance of 2 mm.

To measure the size and distribution of precipitates, cross-sections of the samples were prepared and analyzed with a dual beam scanning electron microscope (Helios G4 P-FIB UXe, Thermo Fisher Scientific, USA) equipped with a Xenon plasma focused ion beam (P-FIB). Protective Pt (mixed with 1.0 wt % C) layers were first deposited on the polished surfaces of samples. Then, trenches were machine polished by the P-FIB.

Transmission electron microscopy (TEM) images were taken by FEI cubed titan Cs-corrected 80–300 kV transmission electron microscope and FEI Talos F200X scanning transmission electron microscope STEM. For the samples before thermomechanical tests, pre-sample preparation consisted of cutting and sawing a NiTi cylinder followed by mechanical polishing to around 20 μm thickness. Then, the thin foils were punched into discs with a diameter of 2.3 mm and glued on 3 mm Cu rings and subsequently milled to electron transparency by Ar ion. For the samples after thermomechanical tests, TEM foil samples were prepared by a Focused Ion Beam (FIB; FEI Helios 600i).

X-ray diffraction (XRD) analysis was carried out for phase identifications and phase fraction calculations in the as-fabricated and post-heat-treated samples. The measurements were carried out using the Bruker D8 Advance diffractometer in Cu-Kα radiation. The step size used was 0.03° in a 2θ range of 17–120° with 45 kV voltage and 40 mA

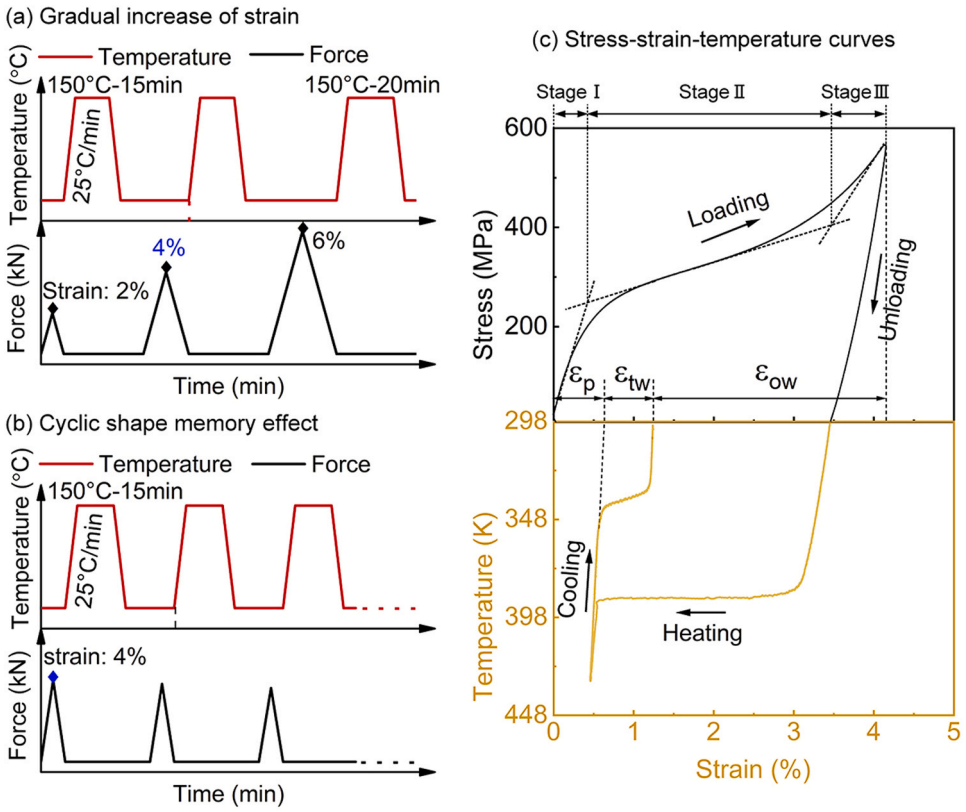

Fig. 2. Schematics of (a) shape memory effect test with gradually increased strain and (b) cyclic shape memory effect, and (c) stress-strain-temperature curves, where ε_p is plastic strain, ε_{ow} is one-way shape memory strain and ε_{tw} is the two way shape memory strain.

current.

Phase transformation behavior was analyzed by differential scanning calorimetry (DSC, Perkin Elmer DSC 8000) in a nitrogen atmosphere, with a cooling and heating rate of 10 K min^{-1} over a temperature range of 203–473 K. DSC samples with a dimension of ϕ 6 × 1 mm were prepared by EDM.

3. Results

3.1. Hardness and microstructure

Vickers hardness was used as a first indication of the effect of different heat treatments on NiTi properties. Fig. 3(a) shows the Vickers hardness variations of L-PBF NiTi with different heat treatment conditions. After heat treatments, all samples show higher hardness than the as-fabricated material (197 HV_2). The solutionized annealed (S) sample shows the smallest hardness deviation among all samples, indicating microstructural/chemical homogeneity. The sample after solutionized annealing (1223 K + 5.5 h) followed by aging (623 K + 18 h), referred to as S+A, has the highest hardness of 226 HV_2.

Since a higher hardness value usually indicates a greater strength [34,35], implying a stronger ability of materials to resist deformation and dislocation movements and proliferation. Hence, to improve NiTi OWSME degradation resistance, a higher hardness is desirable. Based on the hardness results for different aging durations (Fig. 3(b)), 18 h is considered as the optimized aging time after solutionized annealing (Fig. 3(a)), With changing the aging time from 0.5 to 18 h, the hardness increases from ~210–226 HV_2. Increasing further the aging time to 27 h, results in a hardness decrease (from 226 to 218 HV_2), indicating an overaging effect. Therefore, the 18 h aging is considered as a peak aging time resulting in the highest hardness among all the test aging durations.

Optical micrographs of L-PBF NiTi with different heat treatment conditions are shown in Fig. 4. The top-view image of the as-fabricated sample shows a checkerboard grain structure with ~116 μm average grain size (Fig. 4(a)), which results from a bidirectional scanning strategy and epitaxial grain growth within the same deposition layer [36]. The cross-sectional image (viewed along building direction (BD)) displays a columnar structure with curved austenitic grain boundaries (Fig. 4(e)). Such columnar grains grow nearly along BD over several deposition layers, showing a typical epitaxial grain growth [36]. Fig. 4 (b–d) and (f–h) shows the microstructures of heat-treated samples from the top view and cross-section along the BD. Checkerboard grain structures from the top surface and columnar grain structures from the cross-sectional view remain after heat treatments, implying good thermal stability of the L-PBF NiTi samples. During solutionized annealing, the application of high temperature induces the Ostwald ripening phenomenon, resulting in the enlargement of grains [36] (Table 2).

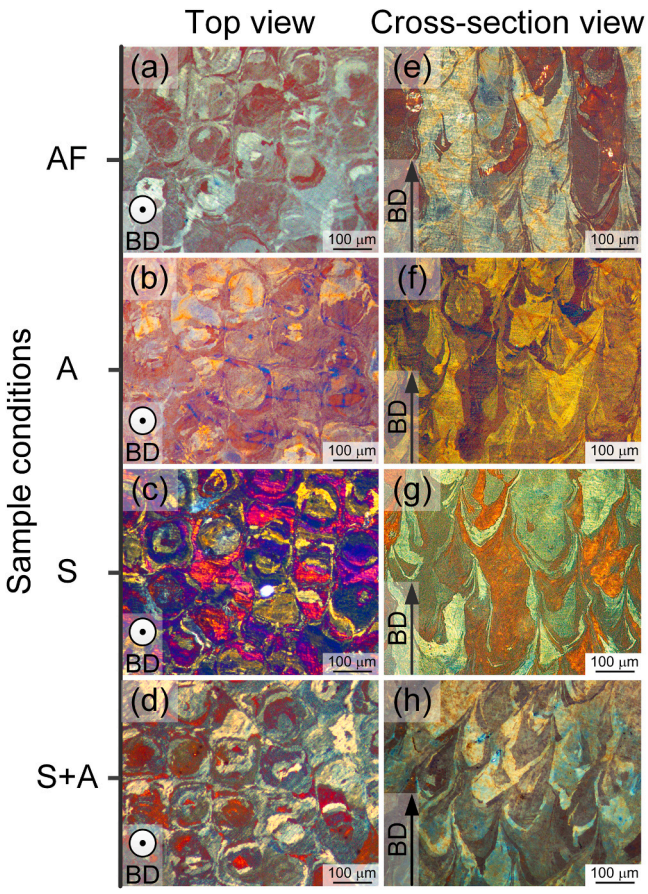

Fig. 4. Optical microscopy images under polarized light from the top and cross-sectional views: (a) and (e) AF, (b) and (f) A, (c) and (g) S, (d) and (h) S+A L-PBF NiTi; Images (a)–(d) showing microstructures from the top view perpendicular to the building direction (BD), and (e)–(h) cross-sectional microstructures along the BD.

Table 2
Comparison of grain sizes after heat treatments.

HT conditions	Grain size in the scanning direction (μm)	Grain size in the perpendicular direction (μm)
AF	116 ± 4	160 ± 7
A	117 ± 5	172 ± 10
S	118 ± 3	184 ± 9
S+A	118 ± 5	196 ± 11

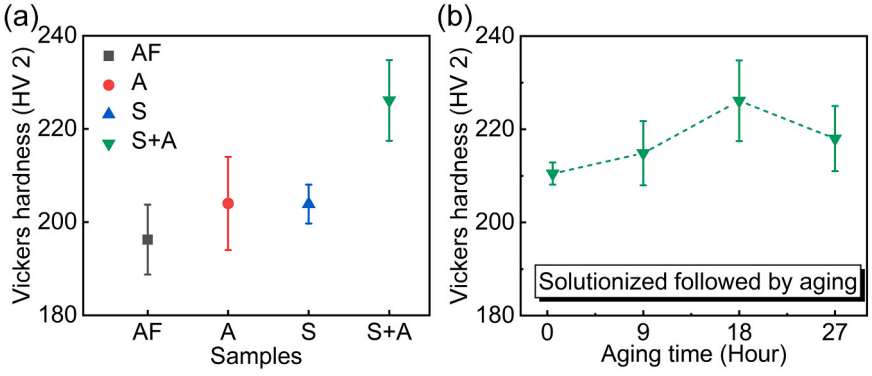

Fig. 3. Vickers hardness for (a) different heat treatment conditions and (b) solutionized (1223 K + 5.5 h) L-PBF NiTi as a function of aging time at 623 K.

3.2. Phase transformation and phase identification

DSC curves, including initial NiTi powder, AF and samples with different heat treatments, are shown in Fig. 5(a), while their corresponding phase transformation temperatures (PTTs) are shown in Fig. 5 (b). The NiTi powder has a broadened phase transformation temperature than other studied herein materials (Fig. 5(a) and (b)), which is attributed to the inhomogeneity of composition and particle size of NiTi powder [37]. Compared with the powder, the as-fabricated L-PBF sample has higher austenite start (A_s) and martensite finish (M_f) temperatures. This results from the lower Ni content due to the evaporation of nickel during the L-PBF process, which has been demonstrated in our previous work [32]. All heat treatment procedures cause an increase in PTTs compared with the AF NiTi (Fig. 5(b)). The solutionized sample (S) shows the highest PTTs and the subsequent aging of the solutionized sample (S+A) decreases the PTT by ~ 5 K (Fig. 5(b)).

As seen in Fig. 5(c), only NiTi austenite (BCC_B2) and martensite (B19′) phases were detected by XRD in the as-fabricated and heat-treated samples, indicating that oxidation was effectively avoided. It also should be mentioned that EDS analysis were carried out on all samples and there is almost no change in Ni and Ti content, which further demonstrates the avoidance of oxidation during heat treatments.

3.3. The effect of aging time on precipitation in solutionized L-PBF NiTi

FIB was employed to polish the samples' cross sections to reveal precipitates in the samples with solutionized annealing followed by different aging times, as shown in Fig. 6. With increasing aging time from 0.5 to 27 h, average sizes of the precipitates increase from ~140–350 nm (Fig. 6). Aging for 18 h results in the highest measured hardness value (Fig. 3(b)). The growth of the precipitates in the sample with 27 h aging is accompanied by a loss in hardness (Figs. 6 and 3(b)).

3.4. Precipitates characterization in as-fabricated and heat-treated L-PBF NiTi

As shown in the high-angle annular dark-field scanning transmission electron microscopy (HAADF-STEM) image, particles are dispersedly distributed within the matrix in the as-fabricated L-PBF NiTi. Particles were indexed as a pure Ti phase based on HRTEM and the corresponding fast Fourier transform (FFT) image. The formation of Ti particles in the matrix is attributed to the high solidification rate during L-PBF, where Ti solute gets trapped in the matrix. Ti particles were barely seen in the Ti-rich NiTi fabricated by conventional methods, such as casting and rolling, since these techniques do not induce a sufficiently high cooling rate. By contrast, the Ti_2NiO_x phase is commonly seen in NiTi fabricated by conventional techniques [17,38,39].

Direct aging (A) promotes the formation of Ti_2NiO_x precipitates (Fig. 8). Ti_2Ni crystal structure is determined by HRTEM and the corresponding FFT pattern (Fig. 8(d) and (e)). It should be noted that the presence of oxygen was confirmed by EDS mappings (Fig. 8(f)). Since oxygen has a certain solubility in Ti_2Ni [38], Ti_2NiO_x forms in directly aged L-PBF NiTi.

After 5.5 h of solutionized annealing under 1223 K, the NiTi sample shows clear martensite phase boundaries, and most precipitates are dissolved in the matrix (Fig. 9(a)). Typical $\{1\bar{1}1\}$ type I martensite twins (mirror symmetry between twin martensite variants) were found in the sample (Fig. 9). The clear martensite twin boundaries and wide

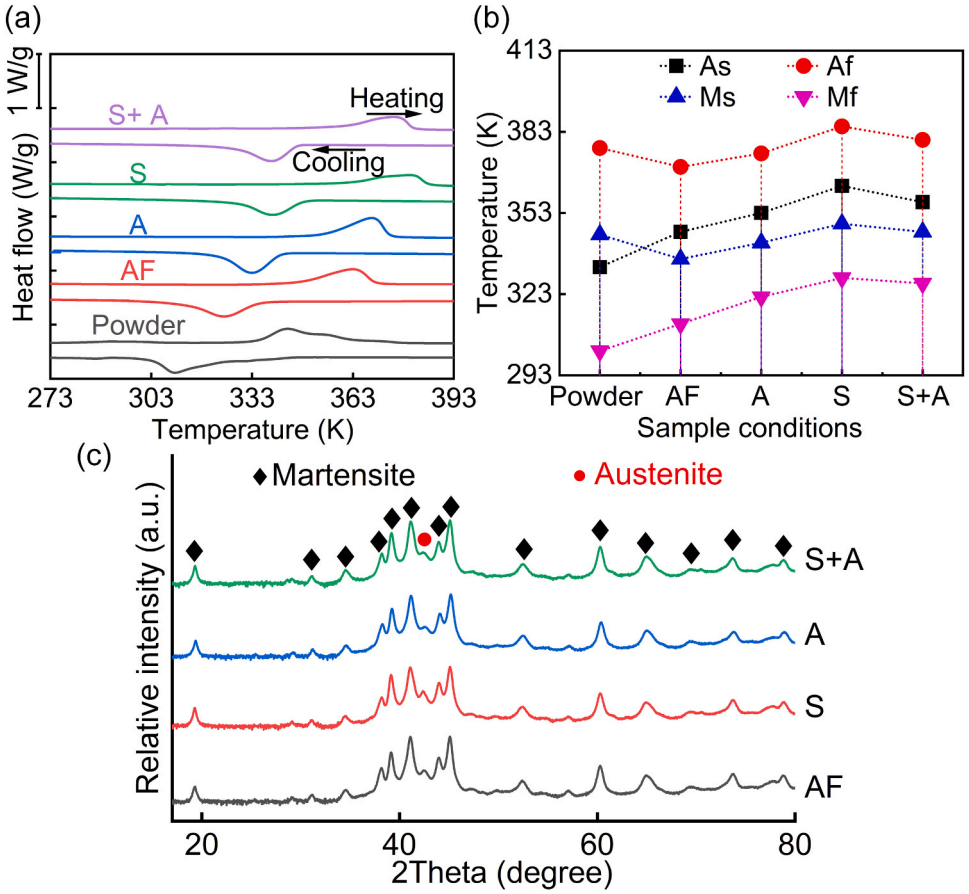

Fig. 5. (a) DSC curves of NiTi powder and L-PBF NiTi for different heat treatment conditions, and (b) corresponding phase transformation temperatures (A_s austenite start temperature, A_f: austenite finish temperature, M_s: martensite start temperature and M_f: martensite finish temperature); (c) X-ray diffraction patterns of L-PBF NiTi without and with different heat treatment conditions.

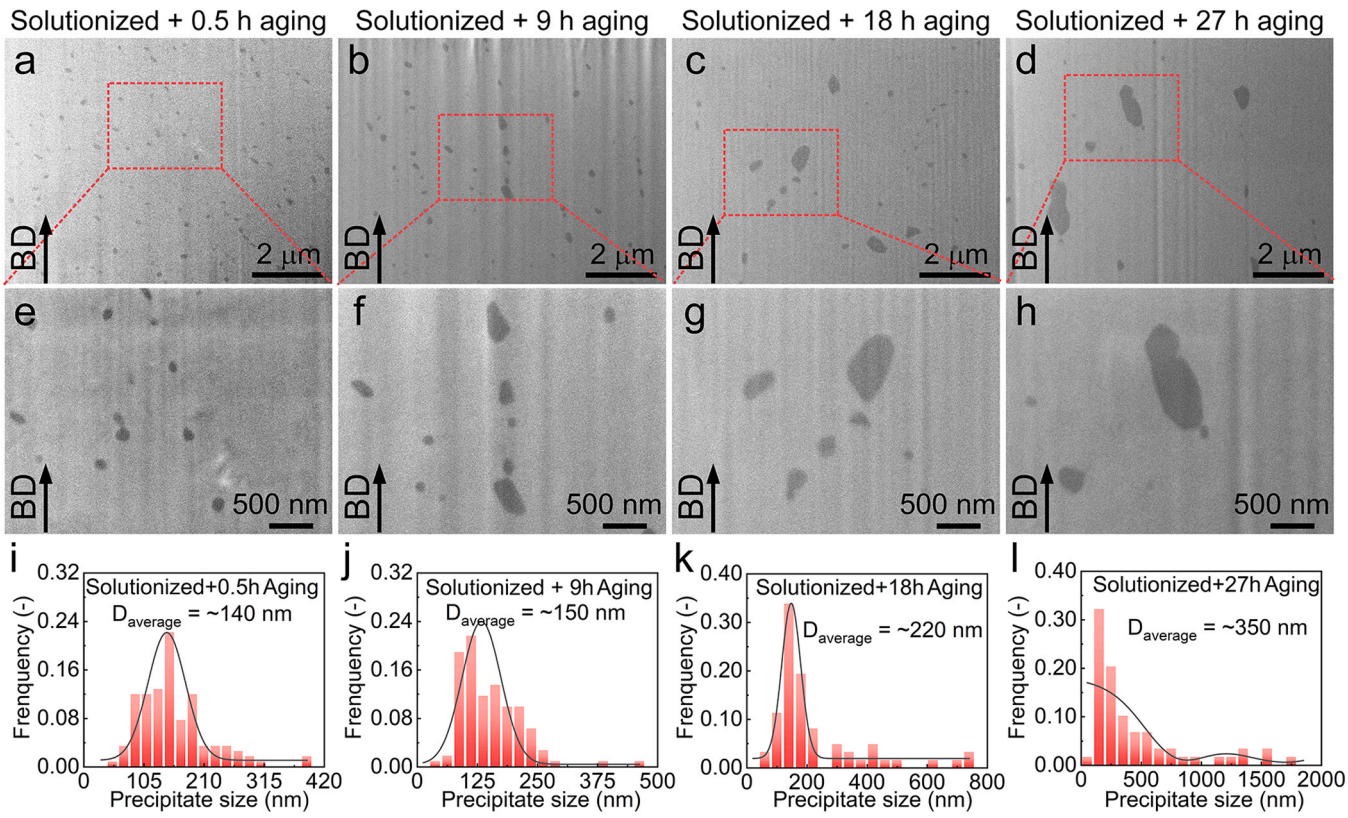

Fig. 6. Cross-sectional SEM-FIB samples after solutionized annealing (1223 K + 5.5 h) followed by 623 K aging with different aging durations: (a), (e) and (i) 0.5 h; (b), (f) and (j) 9 h; (c), (g) and (k) 18 h; (d), (h) and (l) 27 h;.

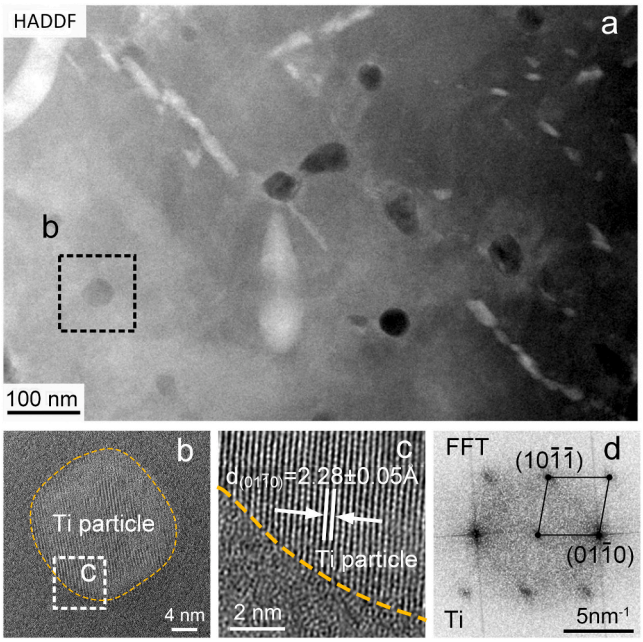

Fig. 7. TEM of as-fabricated L-PBF NiTi sample: (a) HAADF-STEM; (b) HRTEM of precipitate Ti and corresponding (c) enlargement and (d) FFT.

martensite laths indicate the relief of residual stresses and homogenization of the microstructure after solutionized annealing.

The 18 h aging of solutionized NiTi promotes intergranular precipitation (Fig. 10 (a)). Based on the HRTEM and EDS results, the intergranular precipitates are identified as Ti_2NiO_x (Fig. 10 (b)–(f)). Since grain boundaries are high-energy regions, the oversaturated Ti in NiTi matrix tends to precipitate along grain boundaries in a form of a Ti_2Ni-like phase. The Ti_2Ni can be further stabilized by oxygen to form the Ti_2NiO_x phase (Fig. 10 (d)) [16].

3.5. Shape memory behavior

Fig. 11 (a–d) shows the stress-strain curves of all samples under gradually increased strain levels. Thermo-mechanical behavior of all samples consists of three deformation stages [40], including the elastic deformation of twinned martensite (stage I), detwinning and martensite reorientation (stage II) and the elastic deformation of detwinned martensite (stage III) (Fig. 11 (a–d) the corresponding deformation stages has been illustrated in the Fig. 2(c)). Work hardening occurs in all samples, indicating accumulation of dislocations during compression tests. The accumulated dislocations impede phase transformation-induced shape recovery during heating and cause plastic deformation [41]. The recovery ratio of all samples is given in Fig. 11 (e) and shows that different heat treatments barely affect shape memory recovery. It should, however, be noted that heat treatments do improve the maximum true stress under the same strain level (Fig. 11 (f)).

The AF sample has the lowest stress value, with a peak stress of ~844 MPa. Due to the high heating and cooling rate, thermal residual stress can be present in the AF sample, which may provide additional stress for detwinning and martensite reorientation [42]. The aging treatment slightly increases the stress due to the formation of Ti_2NiO_x particles. Solution annealing induces Ti dissolution into the NiTi matrix, which provides solid solution strengthening for NiTi. Therefore, an increased stress is shown in the S sample compared with AF L-PBF NiTi. The S+A sample shows the highest stress for all strain levels and its peak stress reaches 935 MPa, which is in good agreement with observed hardness trends (Fig. 3(a)). The high stress is likely attributed to the formation of Ti_2NiO_x intergranular precipitates and related precipitation

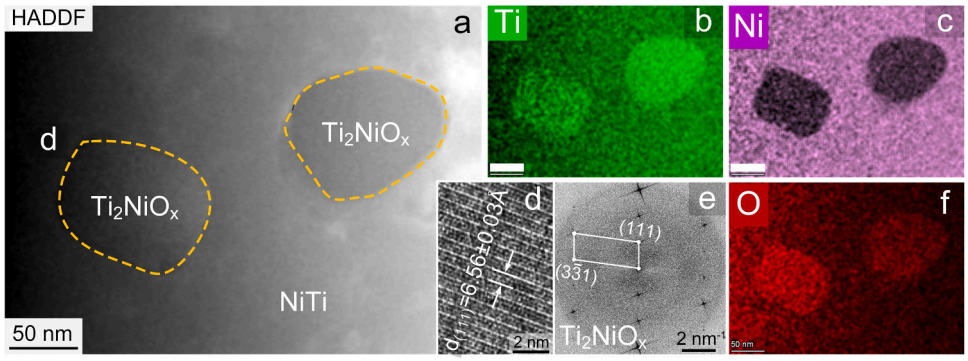

Fig. 8. TEM images of directly aged for 18 h NiTi sample under 623 K: (a) HAADF-STEM; Corresponding EDS mapping: (b) Ti, (c) Ni and (f) O; (d) The HRTEM of precipitate Ti_2NiO_x and (d) its FFT.

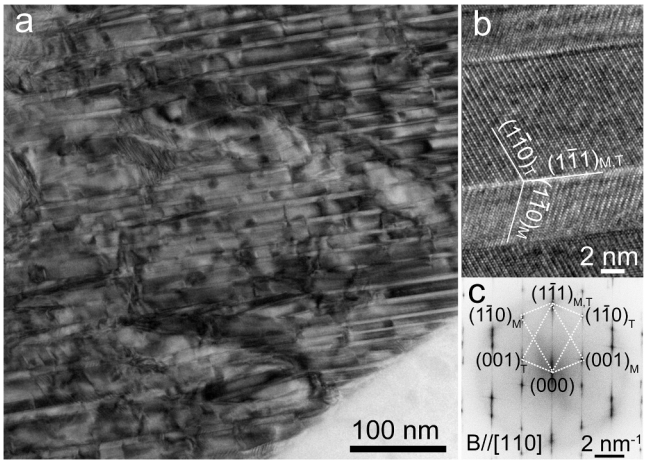

Fig. 9. TEM images of S NiTi sample (1223 K + 5.5 h): (a) BF-TEM image, (b) typical type I twin martensite and (c) corresponding FFT images.

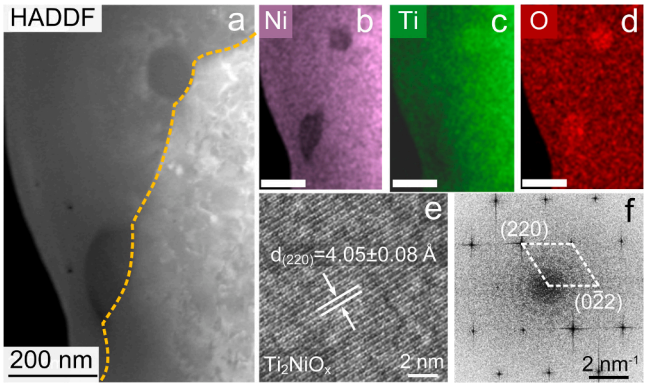

Fig. 10. TEM images of the S+A sample K: (a) HAADF-STEM and corresponding EDS mapping: (b) Ti, (c) Ni and (d) O; (e) The HRTEM of intergranular precipitate of Ti_2NiO_x and (f) its FFT.

hardening.

3.6. Shape memory cyclic stability and two-way shape memory effect

To investigate shape memory degradation and TWSME, cyclic thermo-mechanical tests were carried out on samples with a nominal 4 % engineering strain and 50 cycles. This strain level was chosen because 4 % strain corresponds to a strain where detwinning is completed and the onset of elastic deformation of detwinned martensite exists (Fig. 11).

As shown in Fig. 12, with cyclic thermo-mechanical tests (loading-unloading-heating-cooling-repeat), all samples show the degradation of the shape memory effect and accumulation of irrecoverable strain. During cooling, the strain shows non-linear changes, indicating the two-way shape memory effect (Fig. 12) [43]. The two-way shape memory strain increases with the number of cycles.

As reported by Haberland et al., the conventionally processed NiTi degrades its OWSME to ~1.8 % already within 15 cycles, even at a lower compression stress level (400 MPa) [44]. The solutionized NiTi reported in this study shows the highest shape memory degradation resistance and has ~1.8 % recoverable strain (Fig. 13) even after 50 thermo-mechanical cycles. By contrast, the S+A sample study herein exhibits the lowest recoverable strain (~0.8 %) after 50 thermo-mechanical cycles. The as-fabricated and directly aged NiTi have a similar shape memory degradation behavior (Fig. 13), showing ~1.2 % and 1.1 % recoverable strains after 50 cycles, respectively.

The TWSME strain as a function of thermo-mechanical cycles is shown in Fig. 14. The S+A sample shows the most pronounced two-way shape memory response, and its TWSME strain reaches to ~1.9 % after 50 thermomechanical cycles. However, the solutionized sample, exhibiting the highest shape memory degradation resistance, has the lowest TWSME strain (~1.1 % after 50 cycles). The directly aged NiTi has a slightly higher TWSME strain (~1.4 %) than the as-fabricated NiTi (~1.2 %), which is an intermediate value. By comparing results of OWSME and TWSME strains, opposite trends can be observed. It indicates a direct correlation between shape memory degradation and two-way shape memory evolution, which is further discussed in Section 4.3. It is important to note that the OWSME strain has decreased when taking the cooling-induced TWSME into account. However, in previous studies [30,45], only the heating-strain curves instead of the heat-cooling-strain curves has been shown (Figs. 11 and 12). Therefore, the reported OWSME strains are usually overestimated.

4. Discussion

4.1. Effect of heat treatment on phase transformation temperatures

Fig. 3(a) illustrates the difference in hardness among the samples subjected to various heat treatments. Direct aging leads to an approximate 10 HV_2 increase in hardness compared to the as-fabricated samples. Since Ti particles in the as-fabricated NiTi is in the metastable state (Fig. 7), the direct aging promotes the formation of Ti_2NiO_x precipitates (Fig. 8), resulting in effective precipitation strengthening. Solutionized annealing also yields a similar hardness increment to direct aging (Fig. 3 (a)), but the underlying strengthening mechanism differs. In the solutionized annealed sample, the enhanced hardness is primarily attributed to solid solution strengthening since most precipitates dissolve in the matrix (Fig. 9). Meanwhile, the S+A sample demonstrates the highest hardness increase (~29 HV_2) due to the heat treatment's ability

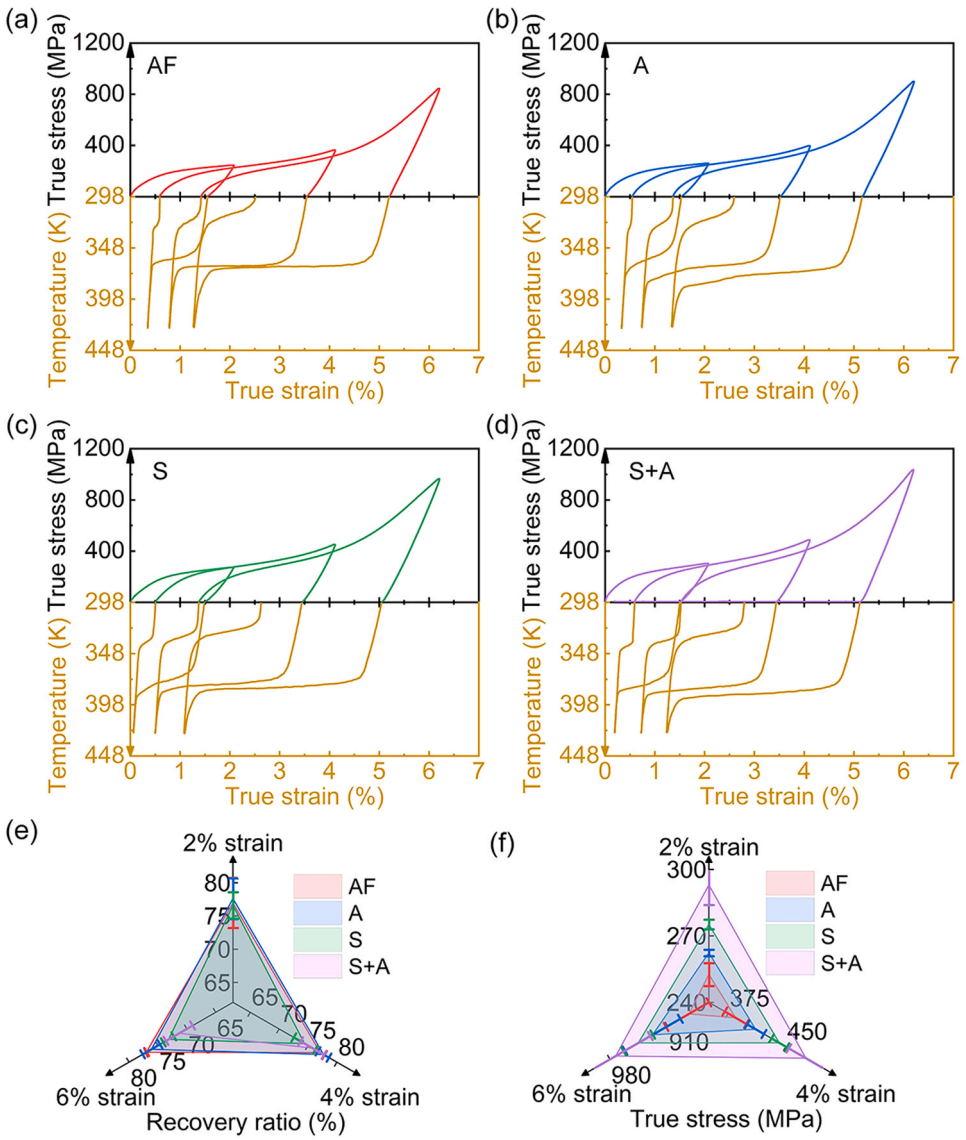

Fig. 11. Stress-strain curves under gradually increased strain level, and corresponding recovery ratio and maximum stress. (a) AF, (b) A, (c) S, (d) S+A, (e) recovery ratio, and (f) maximum true stress.

to promote nanoscale intergranular precipitates of Ti_2NiO_x (Fig. 10). These precipitates play a dual role by contributing to precipitation strengthening and strengthening grain boundaries, effectively pinning dislocations.

4.2. Effect of heat treatment on phase transformation temperatures

Directly aged L-PBF NiTi (A) shows increased phase transformation temperatures (Fig. 5(a) and (b)). Based on the TEM results, direct aging promotes the formation of Ti_2NiO_x (Fig. 8). Since pure Ti particles are the main precipitates in as-fabricated NiTi, direct aging makes Ni in NiTi matrix react with pure Ti to form the Ti_2Ni phase. Furthermore, Ti_2Ni is further stabilized by oxygen to form Ti_2NiO_x. As described above, it results in a decrease of Ni content in NiTi and an increased phase transformation temperature [16].

Solutionized annealing of NiTi leads to higher phase transformation temperatures. This is attributed to 1) the dissolution of Ti and 2) the reduction of atomic-scale defects (such as voids and dislocations). The dissolved Ti causes a decreased Ni/Ti atomic ratio in the NiTi matrix, hence, increasing phase transformation temperatures [16]. Atomic-scaled defects inhibit martensite phase transformation, which can lower transformation temperatures [11]. A high annealing temperature (1223 K) allows NiTi to evolve to a more equilibrium state by eliminating or minimizing atomic defects. Therefore, the solutionized sample shows a further increase in phase transformation temperature.

Subsequent aging of solutionized NiTi slightly decreases its phase transformation temperature (Fig. 5(b)). Since aging promotes intergranular precipitation of Ti_2NiO_x (Fig. 10), more Ti is precipitated than Ni. The Ti comes from the over-saturated Ti in NiTi matrix, which is induced by solutionized annealing followed by water quenching. Therefore, the increase in the Ni/Ti atomic ratio is the main reason for the decreased phase transformation temperatures.

4.3. Shape memory cyclic stability

The results described in Section 3.6 shows that heat treatment dramatically affects L-PBF NiTi shape memory stability and two-way shape memory evolution. To understand the effect of various precipitates and microstructures on the thermomechanical properties of NiTi, TEM was carried out on samples after thermomechanical testing (Fig. 15).

The directly aged NiTi shows intermediate shape memory cyclic

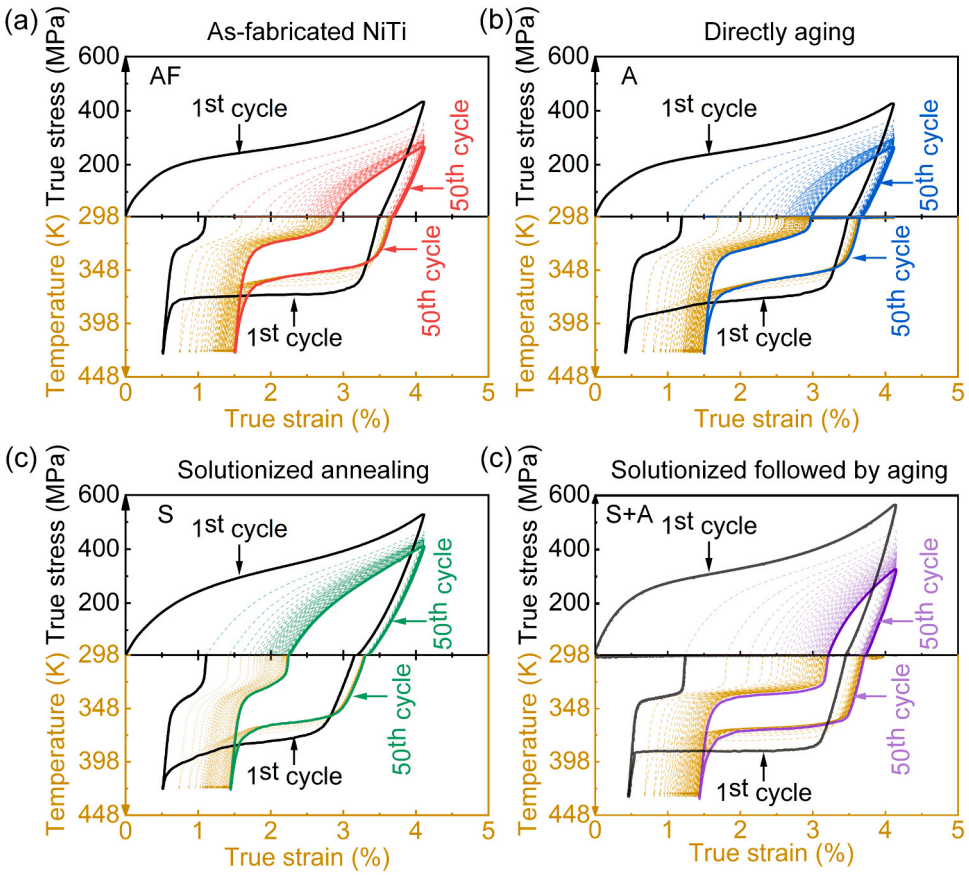

Fig. 12. Stress-strain-temperature curves for 50 cycles under 4 % deformation for (a) AF, (b) A, (c) S and (d) S+A.

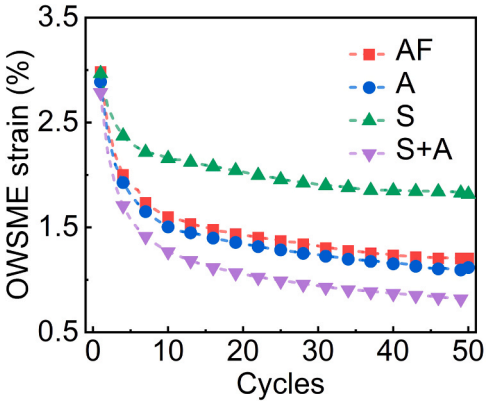

Fig. 13. One-way shape memory effect (OWSME) strain as a function of cycles, under 4 % engineering strain deformation.

stability and TWSME among all tested samples (Figs. 12 and 14). Direct aging promotes Ti_2NiO_x formation within the NiTi matrix, which is an energy barrier for detwinning and martensite reorientation. After 50 cycles of shape memory testing, martensite variants become re-orientated along the loading and unloading direction (Fig. 16). Notably, re-orientated martensite phase boundaries are decorated by precipitates (Fig. 16). As precipitates create local lattice distortions, the mobility of martensite phase boundaries is limited. Hence, re-oriented martensite boundaries are pinned by nano-scaled precipitates. Since the direct aging was carried out at 623 K, which is lower than the typical recrystallization temperature of NiTi (~873 K) [46], dislocation and other meta-structures cannot be fully eliminated. Although direct aging promotes the formation of Ti_2NiO_x, the size of precipitates is ~45 nm, which is similar to the ones in the as-fabricated sample (~36 nm). Hence, the directly aged sample shows similar thermomechanical behavior, i.e., comparable OWSME and TWSME after 50 cycles (Figs. 13 and 14). An increased phase transformation temperature in the directly aged sample is associated with the formation of Ti_2NiO_x.

As shown in Figs. 12–14, the S sample has the highest OWSME degradation resistance and correspondingly exhibits the lowest TWSME recoverable strain after 50 thermomechanical cycles. Since solutionized annealing was carried out at 1223 K, higher than the recrystallization temperature of NiTi, dislocations, meta-structures and residual stresses can be effectively eliminated. This is reflected by the large size of martensite and precipitate-free martensite twin boundaries (Fig. 9). In addition, high-temperature solutionized annealing followed by water quenching also causes the dissolution of precipitates (solid-solution Ti). During thermomechanical cycles, the irrecoverable strain originates from the irreversible plastic deformation and the accumulation of the residual martensite phase. Solutionized annealing decreases the density of dislocations and metal-structures, which reduces irreversible plastic deformation induced by dislocation proliferation. This also can be demonstrated by the STEM-HAADF image of solutionized sample after 50 thermomechanical cycles, where dislocations are barely seen. Its irrecoverable strain is mainly associated with the accumulation of residual detwinned martensite phases. As shown in Fig. 17 (a)–(c), detwinned martensite is still present in the sample after heating to 423 K (higher than its $A_f \approx 386$ K), indicating that the transformation from detwinned martensite to austenite is suppressed. Therefore, the irreversible strain in the solutionized sample is attributed to the accumulation of irreversible martensite. Interestingly, the irreversible detwinned martensite phases appear near the undissolved large-size precipitates (Fig. 17). Such precipitates create internal stress and inhibit phase transformation from detwinned martensite to austenite.

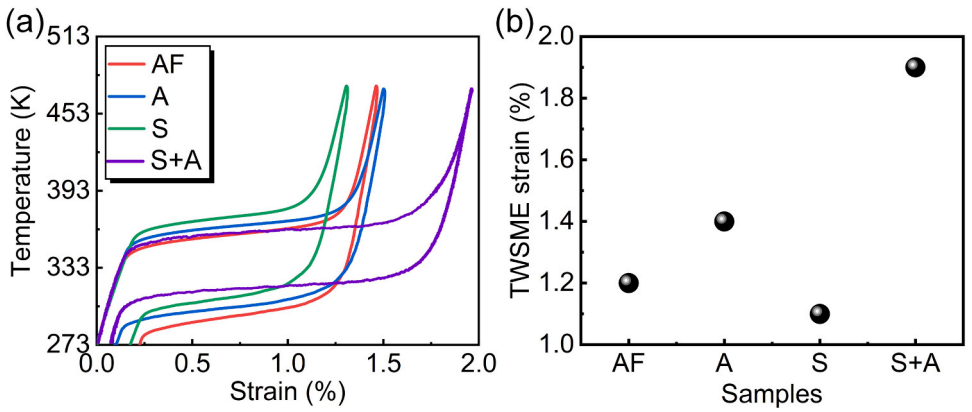

Fig. 14. (a) Strain-temperature curves showing two-way shape memory effect (TWSME) of all samples after 50 thermomechanical cycles, and (b) the corresponding TWSME strains of different samples.

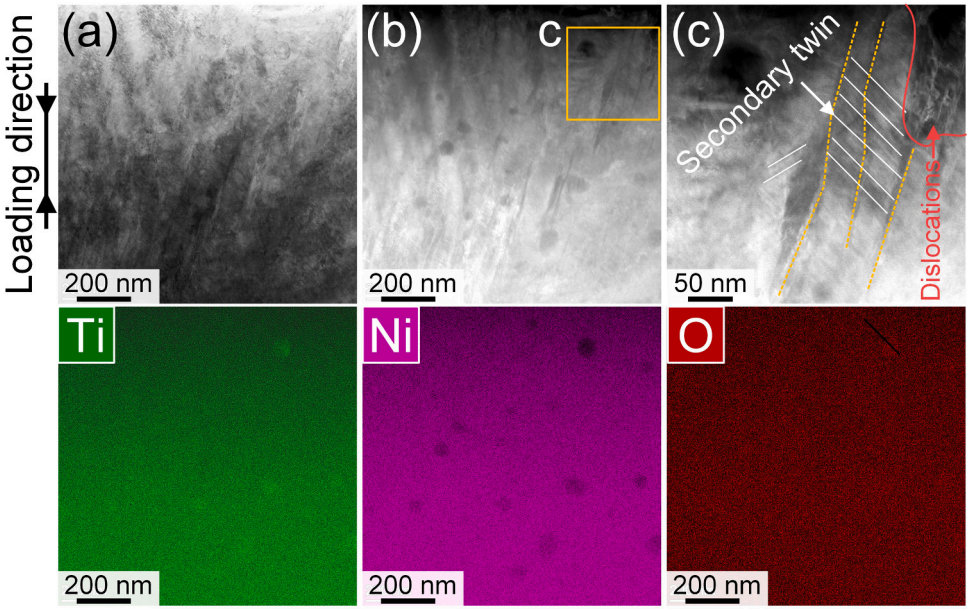

Fig. 15. TEM images of as-fabricated L-PBF NiTi after 50 shape memory cycles: (a) BF image, (b) STEM-HAADF, (c) enlarge zone in (b); The EDS mappings of (a) are shown in the second row.

The S+A sample shows the highest TWSME strain among samples (Fig. 14). The TWSME originates from configured martensite plates by defects and directional internal stress by thermomechanical cycles [47]. It indicates that the S+A sample after thermomechanical cycles has the most effective internal stress state for triggering TWSME.

Such pronounced TWSME response can be attributed to the effective strain partitioning in the S+A sample. As shown in the TEM images of the S+A sample after 50 thermomechanical cycles (Fig. 18), S+A effectively creates a heterogeneous structure around grain boundaries, i.e. nanoscale hard Ti_2NiO_x precipitates and soft NiTi matrix (Fig. 18 (a)–(e)). In addition, due to the existence of Ti_2NiO_x, martensitic transformation in the surrounding NiTi matrix is suppressed. This is confirmed by TEM results. Since the TEM was performed at RT, which is lower than the M_f (~323 K, Fig. 5(a) and (b)), the martensitic phase should have been present rather than the observed austenitic NiTi (Fig. 18 (d)). It has been widely argued that heterogeneous structures can result in strain hardening due to the strain partitioning between soft and hard regions [48–50]. In this case, the S+A sample has the highest stress level under the same deformation among tested samples (Fig. 11). Strain partitioning between NiTi and nanoscale Ni_4Ti_3 has been observed by Dong et al. [51] in Ni-rich NiTi. They demonstrated that nanoscale precipitates, even with a low fraction, still allow for a considerable amount of applied stress. In this work, strain partitioning is induced between nanoscale Ti_2NiO_x and matrix. To the best of the authors' knowledge, this phenomenon is discovered for the first time in Ti-rich NiTi. Since there is a low cooling rate in conventional manufacturing methods, stable and coarse Ti_2NiO_x (several micrometers) precipitates are formed in the as-fabricated state, which cannot be further dissolved within the matrix after high-temperature solutionized annealing [52,53]. By contrast, in this work, nanoscale pure Ti particles are found in as-fabricated Ti-rich L-PBF, which allows for its dissolution into the matrix (Fig. 7) after solutionized annealing. Furthermore, the oversaturated Ti in the matrix precipitates in the form of nanoscale intergranular Ti_2NiO_x in the subsequent aging (Fig. 10).

Therefore, the reason for a large TWSME in the S+A sample results from the as-following two aspects: (1) the hard region, consisting of intergranular Ti_2NiO_x precipitates and surrounding distorted austenite matrix, promotes strain partitioning and makes stress within grains more directional, which is favorable for TWSME; (2) the intergranular Ti_2NiO_x precipitates effectively encloses directional internal stress within each grain, further enhancing TWSME.

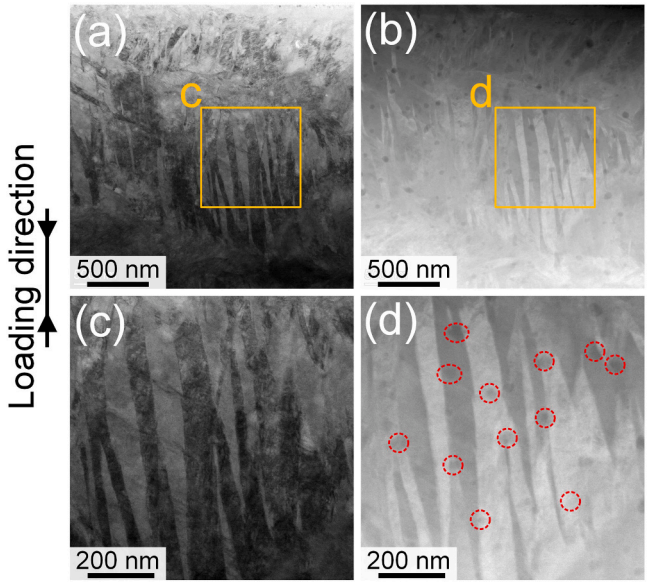

Fig. 16. TEM images of directly aged NiTi after 50 shape memory cycles: (a) and (c) BF image; (b) and (d) STEM-HAADF image (precipitates were marked by red cycles).

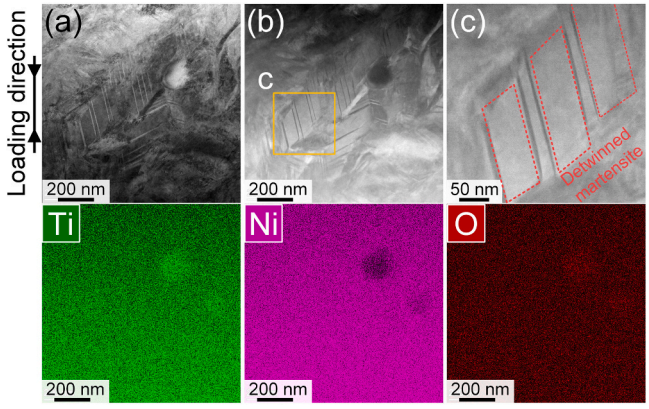

Fig. 17. TEM images of solutionized NiTi after 50 shape memory cycles: (a) BF image, (b) STEM-HAADF image, (c) enlarge zone in (b); The EDS mappings of (a) are shown in the second row.

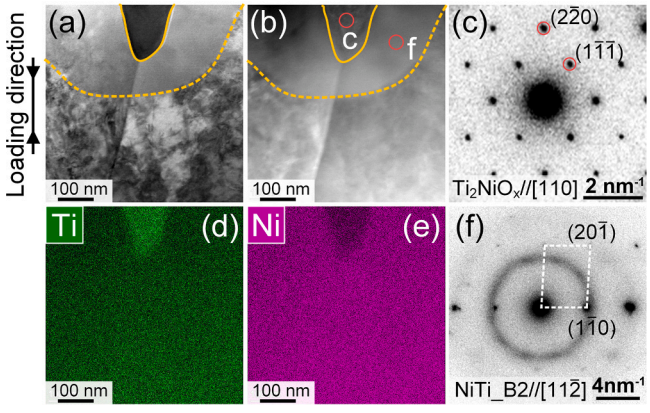

Fig. 18. TEM images of the S+A sample after 50 shape memory cycles: (a) BF image, (b) STEM-HAADF image, (c) SAED of precipitate, (d) and (e) EDS mapping of (a), and (f) SAED of matrix near the precipitate.

5. Conclusions

In this work, the effect of various heat treatments on microstructural evolution, phase transformation, and shape memory behavior was systematically investigated in the L-PBF Ti-rich NiTi. The main conclusions are summarized below:

1. Heat treatments were found to mainly affect nano-scaled precipitates and atomic defects, while grain sizes and morphologies were not significantly affected. Direct aging promotes intragranular precipitation of the Ti_2NiO_x phase, while solutionized annealing dissolves metastable Ti particles into the NiTi matrix and reduces atomic defects. Intergranular Ti_2NiO_x precipitates were shown in the solutionized and aged sample.
2. All heat treatments increase phase transformation compared with those in the as-fabricated state, which was found to be due to an increase in the atomic Ti/Ni ratio in the NiTi matrix and a decrease in atomic defect density.
3. For the single thermomechanical test with gradually increased strain level, the optimized heat treatments allow tailoring the stress window without any sacrifice in the recovery of one-way shape memory strain. For the cyclic thermomechanical tests, solutionized annealing dramatically improved OWSME degradation resistance due to the elimination of microstructural defects, while S+A gave the most pronounced TWSME response due to strain partitioning induced by the heterogonous microstructures between hard intergranular Ti_2NiO_x and soft NiTi matrix.

Relationships between heat treatments, microstructures and functional responses in the L-PBF NiTi are revealed based on multiscale correlative characterization. These findings can be used to enhance the one-way and two-way shape memory degradation resistance of L-PBF NiTi. Furthermore, this work also provides an alternative way to tailor SME temperature and stress windows increasing the attractiveness of 4D-printed NiTi.

CRediT authorship contribution statement

Jia-Ning Zhu: Conceptualization, Methodology, Formal analysis, experimental validation, and Writing – original draft. **Weijia Zhu:** Methodology, Formal analysis, experimental validation, and Writing - review & editing. **Evgenii Borisov:** Methodology, Writing - review & editing. **Xiyu Yao:** Conceptualization, Software, Writing - review & editing. **Ton Riemslag:** Experimental validation, and Writing - review & editing. **Constantinos Goulas:** Experimental validation, and Writing - review & editing. **Anatoly Popovich:** Resources, Writing - review & editing. **Zhaorui Yan:** Methodology and Writing - review & editing. **Frans D. Tichelaar:** Formal analysis, Experimental validation of TEM data collection. **Durga P. Mainali:** Experimental validation, and Writing - review & editing. **M.J.M. Hermans:** Supervision, Resources, Writing - review & editing. **V.A. Popovich:** Conceptualization, Supervision, Resources, Funding acquisition, Project administration, Writing - review & editing.

Declaration of Competing Interest

The authors declare that they have no known competing financial interests or personal relationships that could have appeared to influence the work reported in this paper.

Data Availability

No data was used for the research described in the article.

Acknowledgments

We acknowledge the support from the Russian Science Foundation grant (project No. 19-79-30002). Jia-Ning Zhu wishes to thank the China Scholarship Council (CSC) for its financial support.

References

[1] J. Mohd Jani, M. Leary, A. Subic, M.A. Gibson, A review of shape memory alloy research, applications and opportunities, Mater. Des. 56 (2014) 1078–1113.
[2] A. Ahadi, T. Kawasaki, S. Harjo, W.-S. Ko, Q. Sun, K. Tsuchiya, Reversible elastocaloric effect at ultra-low temperatures in nanocrystalline shape memory alloys, Acta Mater. 165 (2019) 109–117.
[3] X.M. Zhang, J. Fernandez, J.M. Guilemany, Role of external applied stress on the two-way shape memory effect, Mater. Sci. Eng. A 438-440 (2006) 431–435.
[4] T. Omori, J. Wang, Y. Sutou, R. Kainuma, K. Ishida, Two-way shape memory effect induced by bending deformation in ductile Cu-Al-Mn alloys, Mater. Trans. 43 (2002) 1676–1683.
[5] B. Xu, G. Kang, Q. Kan, C. Yu, X. Xie, Phase field simulation on the cyclic degeneration of one-way shape memory effect of NiTi shape memory alloy single crystal, Int. J. Mech. Sci. 168 (2020), 105303.
[6] S.L. Sing, W.Y. Yeong, Laser powder bed fusion for metal additive manufacturing: perspectives on recent developments, Virtual Phys. Prototyp. 15 (2020) 359–370.
[7] Z. Yan, J.-N. Zhu, E. Borisov, T. Riemslag, S.P. Scott, M. Hermans, J. Jovanova, V. Popovich, Superelastic response and damping behavior of additively manufactured Nitinol architectured materials, Addit. Manuf. 68 (2023), 103505.
[8] Y. Guo, Z. Xu, Q. Wang, S. Zu, M. Liu, Z. Yu, Z. Zhang, L. Ren, Corrosion resistance and biocompatibility of graphene oxide coating on the surface of the additively manufactured NiTi alloy, Prog. Org. Coat. 164 (2022), 106722.
[9] Y. Tian, J.A. Muñiz-Lerma, M. Brochu, Nickel-based superalloy microstructure obtained by pulsed laser powder bed fusion, Mater. Charact. 131 (2017) 306–315.
[10] M.-S. Pham, B. Dovgyy, P.A. Hooper, C.M. Gourlay, A. Piglione, The role of side-branching in microstructure development in laser powder-bed fusion, Nat. Commun. 11 (2020) 749.
[11] J.-N. Zhu, E. Borisov, X. Liang, R. Huizenga, A. Popovich, V. Bliznuk, R. Petrov, M. Hermans, V. Popovich, Controlling microstructure evolution and phase transformation behavior in additive manufacturing of nitinol shape memory alloys by tuning hatch distance, J. Mater. Sci. 57 (2022) 6066–6084.
[12] H.R. Kotadia, G. Gibbons, A. Das, P.D. Howes, A review of laser powder bed fusion additive manufacturing of aluminium alloys: microstructure and properties, Addit. Manuf. 46 (2021), 102155.
[13] L. Xu, Z. Chai, B. Peng, W. Zhou, X. Chen, Effect of heat treatment on microstructures and mechanical properties of Inconel 718 additively manufactured using gradient laser power, Mater. Sci. Eng. A 868 (2023), 144754.
[14] T. Pinomaa, M. Lindroos, M. Walbrühl, N. Provatas, A. Laukkanen, The significance of spatial length scales and solute segregation in strengthening rapid solidification microstructures of 316L stainless steel, Acta Mater. 184 (2020) 1–16.
[15] J. Gan, L. Duan, F. Li, Y. Che, Y. Zhou, S. Wen, C. Yan, Effect of laser energy density on the evolution of Ni4Ti3 precipitate and property of NiTi shape memory alloys prepared by selective laser melting, J. Alloy. Compd. 869 (2021), 159338.
[16] J. Frenzel, E.P. George, A. Dlouhy, C. Somsen, M.F.X. Wagner, G. Eggeler, Influence of Ni on martensitic phase transformations in NiTi shape memory alloys, Acta Mater. 58 (2010) 3444–3458.
[17] G. Tadayyon, M. Mazinani, Y. Guo, S.M. Zebarjad, S.A.M. Tofail, M.J.P. Biggs, Study of the microstructure evolution of heat treated Ti-rich NiTi shape memory alloy, Mater. Charact. 112 (2016) 11–19.
[18] A. Falvo, F. Furgiuele, C. Maletta, Two-way shape memory effect of a Ti rich NiTi alloy: experimental measurements and numerical simulations, Smart Mater. Struct. 16 (2007) 771.
[19] T. Simon, A. Kröger, C. Somsen, A. Dlouhy, G. Eggeler, On the multiplication of dislocations during martensitic transformations in NiTi shape memory alloys, Acta Mater. 58 (2010) 1850–1860.
[20] Y. Cao, X. Zhou, D. Cong, H. Zheng, Y. Cao, Z. Nie, Z. Chen, S. Li, N. Xu, Z. Gao, W. Cai, Y. Wang, Large tunable elastocaloric effect in additively manufactured Ni–Ti shape memory alloys, Acta Mater. 194 (2020) 178–189.
[21] S. Saedi, A.S. Turabi, M. Taheri Andani, C. Haberland, H. Karaca, M. Elahinia, The influence of heat treatment on the thermomechanical response of Ni-rich NiTi alloys manufactured by selective laser melting, J. Alloy. Compd. 677 (2016) 204–210.
[22] J. Fu, Z. Hu, X. Song, W. Zhai, Y. Long, H. Li, M. Fu, Micro selective laser melting of NiTi shape memory alloy: Defects, microstructures and thermal/mechanical properties, Opt. Laser Technol. 131 (2020), 106374.
[23] S. Li, H. Hassanin, M.M. Attallah, N.J.E. Adkins, K. Essa, The development of TiNi-based negative Poisson's ratio structure using selective laser melting, Acta Mater. 105 (2016) 75–83.
[24] C. Tan, S. Li, K. Essa, P. Jamshidi, K. Zhou, W. Ma, M.M. Attallah, Laser powder bed fusion of Ti-rich TiNi lattice structures: process optimisation, geometrical integrity, and phase transformations, Int. J. Mach. Tools Manuf. 141 (2019) 19–29.
[25] T.-x Zhao, G.-z Kang, C. Yu, Q.-h Kan, Experimental investigation of the cyclic degradation of the one-way shape memory effect of NiTi alloys, Int. J. Miner., Metall. Mater. 26 (2019) 1539–1550.
[26] L. Orgéas, D. Favier, Stress-induced martensitic transformation of a NiTi alloy in isothermal shear, tension and compression, Acta Mater. 46 (1998) 5579–5591.
[27] Y. Liu, Z. Xie, J. Van Humbeeck, L. Delaey, Asymmetry of stress–strain curves under tension and compression for NiTi shape memory alloys, Acta Mater. 46 (1998) 4325–4338.
[28] Z. Yu, Z. Xu, Y. Guo, R. Xin, R. Liu, C. Jiang, L. Li, Z. Zhang, L. Ren, Study on properties of SLM-NiTi shape memory alloy under the same energy density, J. Mater. Res. Technol. 13 (2021) 241–250.
[29] H.Z. Lu, C. Yang, X. Luo, H.W. Ma, B. Song, Y.Y. Li, L.C. Zhang, Ultrahigh-performance TiNi shape memory alloy by 4D printing, Mater. Sci. Eng., A 763 (2019), 138166.
[30] Q. Zhang, S. Hao, Y. Liu, Z. Xiong, W. Guo, Y. Yang, Y. Ren, L. Cui, L. Ren, Z. Zhang, The microstructure of a selective laser melting (SLM)-fabricated NiTi shape memory alloy with superior tensile property and shape memory recoverability, Appl. Mater. Today 19 (2020), 100547.
[31] N. Shayesteh Moghaddam, S.E. Saghaian, A. Amerinatanzi, H. Ibrahim, P. Li, G. P. Toker, H.E. Karaca, M. Elahinia, Anisotropic tensile and actuation properties of NiTi fabricated with selective laser melting, Mater. Sci. Eng. A 724 (2018) 220–230.
[32] J.-N. Zhu, E. Borisov, X. Liang, E. Farber, M.J.M. Hermans, V.A. Popovich, Predictive analytical modelling and experimental validation of processing maps in additive manufacturing of nitinol alloys, Addit. Manuf. 38 (2021), 101802.
[33] B. Erbstoeszer, B. Armstrong, M. Taya, K. Inoue, Stabilization of the shape memory effect in NiTi: an experimental investigation, Scr. Mater. 42 (2000) 1145–1150.
[34] M.E. Mitwally, M. Farag, Effect of cold work and annealing on the structure and characteristics of NiTi alloy, Mater. Sci. Eng. A 519 (2009) 155–166.
[35] P. Zhang, S.X. Li, Z.F. Zhang, General relationship between strength and hardness, Mater. Sci. Eng. A 529 (2011) 62–73.
[36] T. Bormann, B. Müller, M. Schinhammer, A. Kessler, P. Thalmann, M. de Wild, Microstructure of selective laser melted nickel–titanium, Mater. Charact. 94 (2014) 189–202.
[37] M. Speirs, B. Van Hooreweder, J. Van Humbeeck, J.P. Kruth, Fatigue behaviour of NiTi shape memory alloy scaffolds produced by SLM, a unit cell design comparison, J. Mech. Behav. Biomed. Mater. 70 (2017) 53–59.
[38] J. Mentz, J. Frenzel, M.F.X. Wagner, K. Neuking, G. Eggeler, H.P. Buchkremer, D. Stöver, Powder metallurgical processing of NiTi shape memory alloys with elevated transformation temperatures, Mater. Sci. Eng. A 491 (2008) 270–278.
[39] A. Foroozmehr, A. Kermanpur, F. Ashrafizadeh, Y. Kabiri, Investigating microstructural evolution during homogenization of the equiatomic NiTi shape memory alloy produced by vacuum arc remelting, Mater. Sci. Eng. A 528 (2011) 7952–7955.
[40] Y. Liu, Z. Xie, J.V. Humbeeck, L. Delaey, Y. Liu, On the deformation of the twinned domain in Niti shape memory alloys, Philos. Mag. A 80 (2000) 1935–1953.
[41] C. Yu, G. Kang, Q. Kan, X. Xu, Physical mechanism based crystal plasticity model of NiTi shape memory alloys addressing the thermo-mechanical cyclic degeneration of shape memory effect, Mech. Mater. 112 (2017) 1–17.
[42] Q. Zhou, M.D. Hayat, G. Chen, S. Cai, X. Qu, H. Tang, P. Cao, Selective electron beam melting of NiTi: Microstructure, phase transformation and mechanical properties, Mater. Sci. Eng. A 744 (2019) 290–298.
[43] I. Kaya, H. Tobe, H.E. Karaca, M. Nagasako, R. Kainuma, Y. Chumlyakov, Positive and negative two-way shape memory effect in [111]-oriented Ni51Ti49 single crystals, Mater. Sci. Eng. A 639 (2015) 42–53.
[44] C. Haberland, M. Elahinia, J. Walker, H. Meier, J. Frenzel, Additive Manufacturing of Shape Memory Devices and Pseudoelastic Components (2013).
[45] Z. Xiong, Z. Li, Z. Sun, S. Hao, Y. Yang, M. Li, C. Song, P. Qiu, L. Cui, Selective laser melting of NiTi alloy with superior tensile property and shape memory effect, J. Mater. Sci. Technol. 35 (2019) 2238–2242.
[46] G. Tadayyon, M. Mazinani, Y. Guo, S.M. Zebarjad, S.A.M. Tofail, M.J. Biggs, The effect of annealing on the mechanical properties and microstructural evolution of Ti-rich NiTi shape memory alloy, Mater. Sci. Eng. A 662 (2016) 564–577.
[47] C. Lexcellent, S. Leclercq, B. Gabry, G. Bourbon, The two way shape memory effect of shape memory alloys: an experimental study and a phenomenological model, Int. J. Plast. 16 (2000) 1155–1168.
[48] J. Li, W. Lu, S. Chen, C. Liu, Revealing extra strengthening and strain hardening in heterogeneous two-phase nanostructures, Int. J. Plast. 126 (2020), 102626.
[49] M.N. Hasan, Y.F. Liu, X.H. An, J. Gu, M. Song, Y. Cao, Y.S. Li, Y.T. Zhu, X.Z. Liao, Simultaneously enhancing strength and ductility of a high-entropy alloy via gradient hierarchical microstructures, Int. J. Plast. 123 (2019) 178–195.
[50] F. He, Z. Yang, S. Liu, D. Chen, W. Lin, T. Yang, D. Wei, Z. Wang, J. Wang, J.-j Kai, Strain partitioning enables excellent tensile ductility in precipitated heterogeneous high-entropy alloys with gigapascal yield strength, Int. J. Plast. 144 (2021), 103022.
[51] Y.H. Dong, D.Y. Cong, Z.H. Nie, Z.B. He, L.F. Li, Z.L. Wang, Y. Ren, Y.D. Wang, Stress transfer during different deformation stages in a nano-precipitate-strengthened Ni-Ti shape memory alloy, Appl. Phys. Lett. 107 (2015), 201901.
[52] M. Kaya, A. Buğutekin, N. Orhan, Effect of solution treatment on thermal conductivity of porous NiTi shape memory alloy, Int. J. Thermophys. 32 (2011) 665–673.
[53] C.-l Chu, J.-C.Y. Chung, P.-K. Chu, Effects of heat treatment on characteristics of porous Ni-rich NiTi SMA prepared by SHS technique, Trans. Nonferrous Met. Soc. China 16 (2006) 49–53.